Check for updates

View Article Online
View Journal

Materials Horizons

Accepted Manuscript

This article can be cited before page numbers have been issued, to do this please use: V. Rosciardi, F. Serpe, L. Scozzafava, Y. Promovych, M. Costantini, M. Sasso, C. Sabbatini, R. Angelini and A. Barbetta, *Mater. Horiz.*, 2026, DOI: 10.1039/D6MH00331A.

This is an Accepted Manuscript, which has been through the Royal Society of Chemistry peer review process and has been accepted for publication.

Accepted Manuscripts are published online shortly after acceptance, before technical editing, formatting and proof reading. Using this free service, authors can make their results available to the community, in citable form, before we publish the edited article. We will replace this Accepted Manuscript with the edited and formatted Advance Article as soon as it is available.

You can find more information about Accepted Manuscripts in the Information for Authors.

Please note that technical editing may introduce minor changes to the text and/or graphics, which may alter content. The journal's standard Terms & Conditions and the Ethical guidelines still apply. In no event shall the Royal Society of Chemistry be held responsible for any errors or omissions in this Accepted Manuscript or any consequences arising from the use of any information it contains.

New concepts statement

View Article Online
DOI: 10.1039/D6MH00331A

This work introduces a universal, dual-curing, energy-efficient strategy that enables the high-fidelity 3D printing of thermoset polymers, exemplified here by crosslinked polystyrene. The conceptual shift lies in moving from the need to melt pre-polymerized filaments, as required in Fused Deposition Modeling (FDM), to the extrusion of a colloidal monomer-based ink at ambient temperature. Rapid UV-driven stabilization of a thin external shell of the printed filament is followed by a mild thermal curing of the crosslinked core, allowing the construct to retain its shape throughout printing. This approach represents a breakthrough in currently available 3D printing methods, enabling, for the first time, the direct ink writing of crosslinked polystyrene. A notable outcome of our method is the emergence of superior interlayer adhesion, reflected in mechanical properties exceeding those of benchmark FDM polymers by more than twofold, and in the ability to fabricate challenging overhangs without sacrificial supports. Most importantly, by decoupling printing from polymerization, the method overcomes fundamental kinetic barriers, extending the range of printable materials to virtually any monomer/crosslinker system and enabling continuous multimaterial constructs, even when components exhibit widely different curing kinetics.

Open Access Article. Published on 12 May 2026. Downloaded on 5/15/2026 10:57:01 AM.
This article is licensed under a Creative Commons Attribution 3.0 Unported Licence.

Materials Horizons Accepted Manuscript

View Article Online
DOI: 10.1039/D6MH00331A

Decoupling Shape Retention from Polymerization Kinetics Enables Ambient-Temperature 3D Printing of Polystyrene

Vanessa Rosciardi[†] [a], Federico Serpe[†] [b,c], Luca Scozzafava [b], Yurii Promovych [c], Marco Costantini [c], Marco Sasso [d], Carlo Sabbatini [d], Roberta Angelini* [a], Andrea Barbetta* [b]

[†]: **Vanessa Rosciardi and Federico Serpe equally contributed to this article**

a: Institute for Complex Systems – National Research Council (ISC-CNR) and Physics Department, "La Sapienza" University of Rome, Piazzale Aldo Moro 5, 00185 Rome, Italy

b: Department of Chemistry, "La Sapienza" University of Rome, Piazzale Aldo Moro 5, 00185 Rome, Italy

c: Institute of Physical Chemistry – Polish Academy of Sciences, Marcina Kasprzaka 44/52,01224 Warsaw, Poland

d: Department of Industrial Engineering and Mathematical Sciences, Polytechnic University of Marche, via Brecce Bianche 12, 60131 Ancona, Italy, Italy

Correspondence must be addressed to:

Andrea Barbetta: andrea.barbetta@uniroma1.it; Roberta Angelini: roberta.angelini@cnr.it

Open Access Article. Published on 12 May 2026. Downloaded on 5/15/2026 10:57:01 AM.
This article is licensed under a Creative Commons Attribution 3.0 Unported Licence.

Materials Horizons Accepted Manuscript

View Article Online
DOI: 10.1039/D6MH00331A

Abstract

Polystyrene (PS) is a widely used polymer with numerous structural and functional applications, yet its additive manufacturing remains highly constrained. Conventional Fused Deposition Modeling (FDM) relies on the extrusion of pre-polymerized thermoplastic filaments at temperatures exceeding 230 °C, due to the high softening point of PS, and cannot produce crosslinked architectures. This aspect limits design freedom, energy efficiency, and material performance. Here, we introduce a paradigm-shifting approach for ambient-temperature extrusion of PS using an oil-in-water high internal phase emulsion (HIPE) ink composed of styrene and divinylbenzene dispersed in an aqueous phase. UV irradiation during deposition induces instantaneous crosslinking of the continuous phase, forming a thin hydrogel scaffold that confers structural integrity, while subsequent thermal curing converts the oil phase into dense PS. This dual-curing strategy decouples shape retention from polymerization kinetics, allowing for the printing of complex constructs at room temperature. Compression tests reveal exceptional mechanical performance, with a yield stress comparable to that of benchmark FDM polymers (ABS and PETG) and a maximum compressive stress exceeding their values by more than twofold, highlighting the robustness of interlayer cohesion achieved through in-situ crosslinking. Beyond PS, this versatile approach could unlock new possibilities for scalable, energy-efficient manufacturing of advanced polymer architectures, redefining the boundaries of additive manufacturing.

Open Access Article. Published on 12 May 2026. Downloaded on 5/15/2026 10:57:01 AM.
This article is licensed under a Creative Commons Attribution 3.0 Unported Licence.

Materials Horizons Accepted Manuscript

View Article Online
DOI: 10.1039/D6MH00331A

New concepts statement

This work introduces a universal, dual-curing, energy-efficient strategy that enables the high-fidelity 3D printing of thermoset polymers, exemplified here by crosslinked polystyrene. The conceptual shift lies in moving from the need to melt pre-polymerized filaments, as required in Fused Deposition Modeling (FDM), to the extrusion of a colloidal monomer-based ink at ambient temperature. Rapid UV-driven stabilization of a thin external shell of the printed filament is followed by a mild thermal curing of the crosslinked core, allowing the construct to retain its shape throughout printing. This approach represents a breakthrough in currently available 3D printing methods, enabling for the first time the direct ink writing of crosslinked polystyrene. A notable outcome of our method is the emergence of superior interlayer adhesion, reflected in mechanical properties exceeding those of benchmark FDM polymers by more than twofold, and in the ability to fabricate challenging overhangs without sacrificial supports. Most importantly, by decoupling printing from polymerization, the method overcomes fundamental kinetic barriers, extending the range of printable materials to virtually any monomer/crosslinker system and enabling continuous multimaterial constructs, even when components exhibit widely different curing kinetics.

Open Access Article. Published on 12 May 2026. Downloaded on 5/15/2026 10:57:01 AM.
This article is licensed under a Creative Commons Attribution 3.0 Unported Licence.

Materials Horizons Accepted Manuscript

View Article Online
DOI: 10.1039/D6MH00331A

Open Access Article. Published on 12 May 2026. Downloaded on 5/15/2026 10:57:01 AM.
This article is licensed under a Creative Commons Attribution 3.0 Unported Licence.

Materials Horizons Accepted Manuscript

Introduction

Additive manufacturing has revolutionized polymer processing, enabling the production of complex geometries and customized designs.[1][2] However, this technology remains fundamentally constrained by the nature of the materials it employs.[3] Conventional extrusion-based methods, such as Fused Deposition Modeling (FDM), rely on thermoplastic filaments that must be melted and deposited layer by layer.[4] For amorphous polystyrene (PS), this requires extrusion temperatures exceeding 230°C due to its high softening point (≈ 240°C) and glass transition near 100°C.[5] These conditions not only demand energy-intensive processing but also preclude the formation of crosslinked architectures,[6] limiting dimensional stability and chemical resistance.[7] As a result, PS, despite its ubiquity and desirable properties, has been largely excluded from advanced additive manufacturing workflows.[8]

Recent efforts have sought to overcome limitations imposed by FDM by introducing reactive inks and in-situ polymerization strategies.[9–11] Among these, high internal phase emulsions (HIPEs) have emerged as promising candidates due to their unique rheological behaviour,[12–14] which combines high viscosity with shear-thinning and elasticity, key properties for extrusion printing.[15,16] In our previous work, we demonstrated that HIPEs containing styrene and divinylbenzene (DVB) could serve as stable inks for printing crosslinkable PS-based constructs.[17] This approach represented a paradigm shift, *i.e.,* printing monomers rather than polymers, followed by post-print polymerization. However, the polymerization kinetics of styrene proved incompatible with the fast-printing process, preventing rapid stabilization of the printed filaments. By contrast, in the same study, HIPEs formulated with methacrylate (a blend of methyl methacrylate and hexyl methacrylate) monomers cured almost instantaneously under UV light.

The present work resolves the kinetic bottleneck of styrene through a dual-phase curing strategy (**Figure 1**). By incorporating water-soluble methacrylated dextran (DexMA) in the styrene-based HIPE, we introduce a functionality with fast reactivity (methacrylate)[18] in the external phase, enabling UV-induced crosslinking of an ultra-thin hydrogel scaffold around the styrene droplets in the extruded filament. This instantaneous reticulation provides structural integrity at ambient conditions, decoupling shape retention from polymerization kinetics, a fundamental limitation in printing techniques using monomer-containing inks. Subsequent thermal curing at 60°C completes the polymerization of styrene/DVB within the oil phase, yielding dense, dimensionally stable PS constructs. This innovation transforms

View Article Online
DOI: 10.1039/D6MH00331A

the extrusion printing process from a thermally constrained operation into a modular, room-temperature platform for advanced polymer architectures.

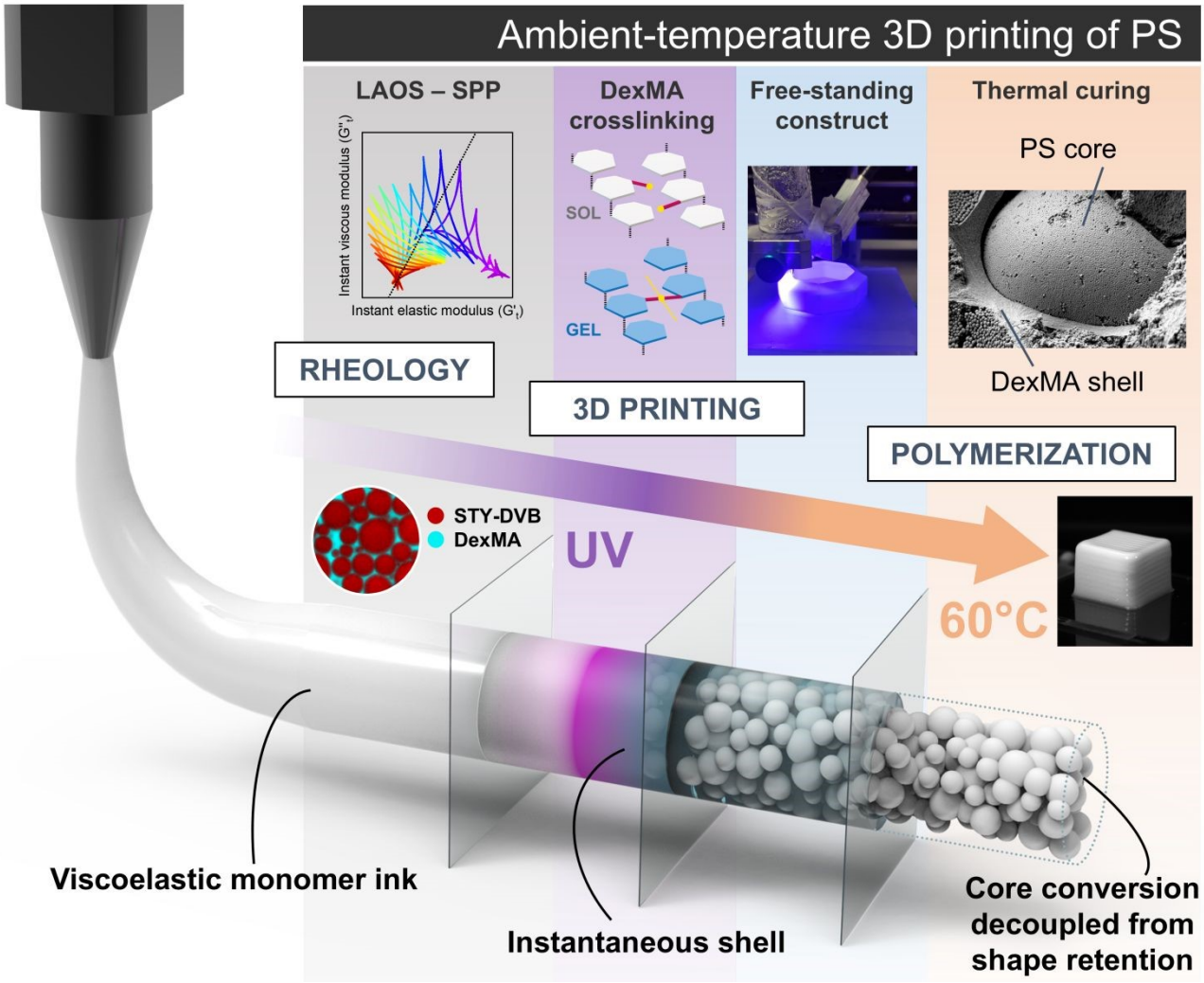

Figure 1. Overview of the ambient-temperature printing strategy for polystyrene (PS) using HIPE-based inks. The process begins with a viscoelastic high internal phase emulsion (HIPE) ink composed of 85% vol/vol styrene-divinylbenzene (STY-DVB) droplets dispersed in a 15% vol/vol aqueous phase containing methacrylated dextran (DexMA). The oil phase contains a thermal radical initiator, while the water phase contains a photoinitiator. The ink exhibits pronounced non-linear viscoelasticity, as characterized through large amplitude oscillatory shear (LAOS) experiments and interpreted using the Sequence of Physical Processes (SPP) framework, a state-of-the-art method for correlating rheological fingerprints with printing performance. The ink is extruded through the printing nozzle. Upon deposition, UV irradiation triggers instantaneous crosslinking of DexMA, forming a thin hydrogel shell around the emulsion droplets. The rapid stabilization decouples shape retention from the slower polymerization kinetics of styrene, enabling the fabrication of free-standing constructs. Finally, thermal curing at 60°C converts the internal oil phase into a dense PS core while preserving the external DexMA shell, yielding a hierarchical architecture.

.

Open Access Article. Published on 12 May 2026. Downloaded on 5/15/2026 10:57:01 AM.
This article is licensed under a Creative Commons Attribution 3.0 Unported Licence.

Materials Horizons Accepted Manuscript

View Article Online
DOI: 10.1039/D6MH00331A

Beyond polystyrene, the implications of this method are profound. Printing monomer-rich inks opens access to a vast library of crosslinked (thermosetting) polymers, which cannot be processed via traditional extrusion techniques.[19,20] Moreover, the modularity of HIPE formulations can support multi-material printing using multiple syringes loaded with distinct monomers or monomer mixtures, enabling gradient structures, compositional heterogeneity, and integrated functionalities within a single construct. Ultimately, this approach eliminates the need for energy-intensive melting processes, thereby reducing operational costs and increasing compatibility with low-cost extrusion platforms, which in turn minimizes infrastructure requirements.

Experimental

Chemicals: Dextran (from *Leuconostoc* spp., $M_w \approx 70000$), dimethyl sulfoxide (DMSO >99% purity), glycidyl methacrylate (GMA, >97% purity), 4-(N,N-dimethylamine)pyridine (DMAP, 99%), hydrochloric acid (HCl), styrene (>99% with 4-tert-butylcatechol as stabilizer), divinylbenzene (80% purity stabilized with 4-tert-butylpyrocatechol), glycerol (>99.5% purity), sodium dodecyl sulfate (SDS, >99% purity), Fluorescein isothiocyanate-dextran (FITC-Dextran, $M_w \approx 70000$), Nile Red, 2,2'-Azobis(2-methylpropionitrile), (AIBN, 98% purity), Lithium phenyl-2,4,6-trimethylbenzoylphosphinate (LAP, >95 % purity), acetone, polystyrene ($M_w \approx 192000$) were all purchased from Merck/Sigma-Aldrich. Deionized water was used for sample preparation and dialysis procedures.

Dextran methacrylation: The preparation of methacrylated dextran (DexMA) was conducted following a protocol reported in the literature.[21,22] Briefly, dextran (40 g) was dissolved in DMSO (360 mL) in a sealed round-bottom flask. After dissolution of DMAP (8.0 g), a calculated amount of GMA (10.5 g, equivalent to a theoretical degree of substitution of 30%) was added. The solution was stirred at room temperature for 48 h, after which the reaction was stopped by adding an equimolar amount of concentrated HCl to neutralize the DMAP. The reaction mixture was transferred into a dialysis tube and extensively dialyzed against demineralized water at 4 °C until the nominal conductivity of water was reached. The solution of DexMA was lyophilized, and the obtained product was stored at 4 °C before use. The degree of vinyl functionalization, as determined by ^{1}HNMR, was 25%.

High internal phase emulsions (HIPEs) preparation: Oil-in-water high internal phase emulsions (HIPEs) were prepared by separately formulating the oil and aqueous phases.

Open Access Article. Published on 12 May 2026. Downloaded on 5/15/2026 10:57:01 AM.
This article is licensed under a Creative Commons Attribution 3.0 Unported Licence.

Materials Horizons Accepted Manuscript

View Article Online
DOI: 10.1039/D6MH00331A

The oil phase consisted of styrene and divinylbenzene (volume ratio 9:1). The aqueous phase consisted of deionized water and glycerol (volume ratio 3:2), with sodium dodecyl sulfate (SDS, 5 wt% relative to the aqueous phase) and DexMA (1, 3, or 5 wt%) dissolved in the water/glycerol mixture. For samples intended for morphological and rheological characterization, no polymerization initiators were added, and monomers were used as received without removing stabilizers. For samples prepared for 3D printing, lithium phenyl-2,4,6-trimethylbenzoylphosphinate (LAP, 0.5% wt/v relative to the aqueous phase) and azobisisobutyronitrile (AIBN, 0.5% wt/v relative to the oil phase) were incorporated. In this case, styrene and divinylbenzene were purified prior to use by passing them through a basic alumina column under mild vacuum to remove polymerization inhibitors. HIPEs were obtained by dropwise addition of the oil phase into the aqueous phase in a flat-bottomed vessel, maintaining a final phase ratio of 85 vol% oil and 15 vol% aqueous phase. Emulsification was performed under magnetic stirring at 450 rpm, followed by an additional 5 min at 600 rpm to ensure complete homogenization.

Morphological analysis: Morphological characterization of HIPEs was performed using confocal laser scanning microscopy (CLSM). Emulsions were stained with Nile Red (oil phase, 15 μg·mL^{-1}) and contained FITC-Dextran in the aqueous phase. Fluorescent images were acquired on an Olympus FV1200 microscope equipped with a solid-state laser (λ = 473 nm and 559 nm) and a photomultiplier tube (PMT) detector (detection range: 485–520 nm for FITC-Dextran and 570-610 nm for Nile Red). A 100× oil-immersion objective (Zeiss) was employed. Samples were mounted in Lab-Tek™ chambered borosilicate cover glass systems (Nalge Nunc International, Rochester, NY, USA) prior to imaging.

Two-dimensional CLSM images were processed using ImageJ software. After binarization with an image-specific threshold, particle analysis was performed via the “Analyze Particles” plugin. Droplet areas were converted to equivalent diameters to calculate the mean droplet size and size distribution, which was visualized as a 3D histogram. The polydispersity index (PDI) of droplet radii was calculated as:[68]

$$PDI(\%) = \frac{\sqrt{\langle r^2{}_{droplet}\rangle - \langle r_{droplet}\rangle^2}}{\langle r_{droplet}\rangle} \cdot 100$$

Linear rheological measurements: Rheological characterization was performed using an Anton Paar MCR302 rheometer equipped with a cone–plate geometry (cone angle: 2°, diameter: 25 mm). The gap between the cone and plate was set to 0.104 mm, and the

Open Access Article. Published on 12 May 2026. Downloaded on 5/15/2026 10:57:01 AM.
This article is licensed under a Creative Commons Attribution 3.0 Unported Licence.

Materials Horizons Accepted Manuscript

View Article Online
DOI: 10.1039/D6MH00331A

temperature was maintained at 22 °C using a Peltier system. An isolation hood was employed to minimize solvent evaporation and sample drying.

Shear-rate-controlled viscosity measurements were conducted over a range of 0.001–1000 s^{-1} following a pre-shear at 500 s^{-1}. Oscillatory tests were performed to determine the storage modulus (*G′*) and loss modulus (*G″*) within the linear viscoelastic region (LVE) and to identify deviations from linearity and crossover points. These tests were carried out at angular frequencies of 1, 5, and 15 $rad \cdot s^{-1}$ with strain amplitudes varying from 0.1% to 1000%, under constant normal force. All measurements were performed in triplicate, and results are reported as mean values.

Non-linear rheology and sequence of physical processes (SPP) approach: Large Amplitude Oscillatory Shear (LAOS) measurements were performed using the same rheometer setup described above, equipped with the Anton Paar RheoCompass™ software and its LAOS analysis module. Amplitude sweep tests were conducted at fixed angular frequency of 5 rad/s, with strain amplitudes ranging from 0.1% to 1000% with a point density of 23. For each imposed strain amplitude, the instrument recorded 513 time-resolved data points corresponding to multiple cycles of sinusoidal strain oscillation from 0 to the maximum strain value ($\boldsymbol{\gamma_{max}}$). The raw dataset for each set of 513 points included time, instantaneous strain $\boldsymbol{\gamma}(t)$, stress $\boldsymbol{\sigma}(t)$, and shear rate $\dot{\boldsymbol{\gamma}}(t)$. These data were analysed through an in-house custom python script (reported in Supporting Information and deposited on GitHub) using the sequence of physical processes (SPP) framework proposed by Rogers.[43] In SPP, the oscillatory response is treated as a space curve in the tree-dimensional deformation space defined by strain, shear rate, and stress, $\boldsymbol{r}(t) = (\boldsymbol{\gamma}(t), \dot{\boldsymbol{\gamma}}(t), \boldsymbol{\sigma}(t))$.The local geometry of this curve is described by the Frenet-Serret frame, which consists of the tangent vector $\vec{\boldsymbol{T}}(t)$, the normal vector $\vec{\boldsymbol{N}}(t)$, and the binormal vector $\vec{\boldsymbol{B}}(t)$,

$$\vec{\boldsymbol{T}}(t) = \frac{\boldsymbol{r}'(t)}{\|\boldsymbol{r}'(t)\|} \qquad \vec{\boldsymbol{N}}(t) = \frac{\vec{\boldsymbol{T}}'(t)}{\|\vec{\boldsymbol{T}}'(t)\|} \qquad \vec{\boldsymbol{B}}(t) = \vec{\boldsymbol{T}}(t) \times \vec{\boldsymbol{N}}(t)$$

The tangent is obtained by normalizing the first derivative of the curve with respect to arc length, the normal by normalizing the derivative of the tangent, and the binormal as the cross product of tangent and normal. These three vectors define the instantaneous orientation of the curve, and the osculating plane spanned by $\vec{\boldsymbol{T}}$ and $\vec{\boldsymbol{N}}$ represents the direction of curvature at each point along the trajectory. Within this osculating plane, the stress evolution is decomposed into components aligned with strain and shear rate, allowing the calculation of

Open Access Article. Published on 12 May 2026. Downloaded on 5/15/2026 10:57:01 AM.
This article is licensed under a Creative Commons Attribution 3.0 Unported Licence.

Materials Horizons Accepted Manuscript

View Article Online
DOI: 10.1039/D6MH00331A

instantaneous elastic and viscous moduli. The projection of the curve's motion onto these directions gives

$$\sigma(t) \approx G_t'\gamma(t) + \eta_t\dot{\gamma}(t) \qquad G_t'' = \omega\eta_t$$

Where G'_t reflects the elastic contribution and G''_t the viscous contribution, with η_t derived from the shear-rate projection. This geometric approach captures the material's nonlinear behaviour throughout each oscillatory cycle without relying on Fourier decomposition. The resulting pairs of G'_t and G''_t for each strain cycle are represented in Cole-Cole plots, providing an intuitive visualization of intracycle transitions between solid-like and liquid like responses.

Printing set-up and printability tests: An in-house 3D printer equipped with an XYZ motor system and a build volume of approximately 10x10x0.3 cm³ was controlled via Pronterface software. The printer features a custom stainless-steel housing with a central aperture and adjustable screw clamps to securely hold the ink-loaded syringe in alignment with the mechanical deposition system. The feed rate of the printer was set to 900 mm/min, unless differently specified. The syringe (20 mL, KDS stainless steel, Sigma-Aldrich) is fitted with a conical stainless-steel nozzle with a minimum tip diameter of 0.7 mm. The housing also includes four equidistant mounts, one for each UV optical fibre, ensuring uniform illumination at the nozzle tip. Ink extrusion is pneumatically regulated through an OB1 MK4 microfluidic flow controller (Elveflow, France) connected to a nitrogen source. UV source is an OmniCure® S2000 Elite system equipped with a high-pressure 200 W mercury vapor lamp. In the employed configuration, four high-power fibre light guides are coupled to the UV source, each conveying an average irradiance of 18 W·cm⁻² to the nozzle tip (5 mm working distance), as determined from the irradiance spectra provided by the manufacturer. For all printing purposes, the power intensity of the UV reaching the nozzle was set to 5%, corresponding to an irradiance of 0.9 W·cm⁻² for each lightguide. Two-dimensional printability was evaluated through filament fusion tests.[50] In this test, a filament of ink was extruded in a serpentine pattern with progressively increasing spacing between adjacent parallel segments. The aim was to determine the critical distance at which neighbouring filaments cease to fuse and remain distinguishable. Three parameters were considered: the axial distance between adjacent filaments (f_d), the filament thickness (f_t), which served as a normalization factor to account for thickness variations, and the fused segment length (f_s), corresponding to the portion where two adjacent filaments merge. The serpentine geometric code (G-code) was programmed with interfibre distances increasing from 0.2 mm to 3.2 mm

Open Access Article. Published on 12 May 2026. Downloaded on 5/15/2026 10:57:01 AM.
This article is licensed under a Creative Commons Attribution 3.0 Unported Licence.

Materials Horizons Accepted Manuscript

View Article Online
DOI: 10.1039/D6MH00331A

in steps of 0.2 mm, following the progression $f_{d(n)} = f_{d(n-1)} + 0.2$ mm. For each sample, three serpentines were printed, photographed orthogonally, binarized, and analysed using ImageJ to calculate f_d, f_t, and f_s. The ratio f_s/f_t was used as a resolution indicator, with values approaching 1 corresponding to the highest resolution and minimal fusion beyond the intended contact points. Results are presented as f_d versus f_s/f_t. Ink flow pressure was adjusted to the minimum value ensuring continuous deposition of an uninterrupted filament, with pressures of 30, 32, 35, and 40 mbar for formulations containing 0, 1, 3, and 5% wt/v DexMA, respectively. These same pressures were applied for 3D printing of cubic samples to assess shape retention and fidelity under conditions with and without UV illumination.

Optimal printing protocol and complex shape printing: After UV-assisted printing of cubic samples, the constructs were subjected to progressively longer post-curing cycles in an AnyCubic Wash and Cure 3 Plus chamber (36 W). This test allowed the determination of the optimal curing time for each formulation, qualitatively assessed by the absence of oil leakage caused by overcuring and network shrinkage of DexMA. For the fabrication of complex constructs, the 5% wt/v DexMA formulation was employed, with printing parameters progressively optimized to enable self-standing, non-planar, and overhanging geometries. The final printing protocol consisted of a pressure of 55 mbar, a feed rate of 675 mm·min^{-1}, UV intensity during printing set to 5%, and post-printing UV curing for 1 min. Afterwards, constructs were placed in oven at 60°C for 6 hours to fully complete the solidification. G-codes for all printed shapes were generated using FullControl G-Code Designer.[69]

Scanning electron microscopy: Polymerized composite constructs based on crosslinked polystyrene were purified via Soxhlet extraction with isopropanol for 24 h to remove the surfactant and non-crosslinked monomers and then dried in an oven at 50°C overnight. The constructs were then mechanically freeze-fractured after immersion in liquid nitrogen to obtain clean internal fracture surfaces. Samples were analysed with a Scanning Electron Microscope (SEM) (Zeiss Auriga, Germany) after cobalt plasma sputtering (Q150T, Quorum Technologie, UK) to create a 25 nm conductive film. Images were acquired using a secondary electron detector at magnifications from 1000x to 40000x.

Mechanical tests: Mechanical compression tests were performed under quasi-static conditions using an electromechanical universal testing machine (Zwick Z50®), equipped with a 50 kN load cell and compression platens compliant with ASTM D695. All tests were carried out at room temperature under laboratory ambient conditions. The machine

Open Access Article. Published on 12 May 2026. Downloaded on 5/15/2026 10:57:01 AM.
This article is licensed under a Creative Commons Attribution 3.0 Unported Licence.

Materials Horizons Accepted Manuscript

View Article Online
DOI: 10.1039/D6MH00331A

crosshead was driven in displacement control at a nominal engineering strain rate of 10^{-3} s^{-1}. The specimens had a nominal parallelepiped geometry, with a square base of 10 mm × 10 mm and a height of 7 mm. Prior to testing, the loading surfaces were carefully machined to ensure flatness and mutual parallelism. A low-friction interface was adopted between the specimen and the compression plates in order to limit friction-induced barreling phenomena. In addition to the force–displacement data acquired by the testing machine, deformation measurements were obtained by means of Digital Image Correlation (DIC). During the tests, images of the specimens were acquired at 25 frames per second using a stereo setup consisting of two high-resolution digital cameras (FLIR Blackfly S BFS-U3-88S6M-C®) equipped with Fujinon CF50ZA-1S lenses. The specimen surface preparation, speckle pattern characteristics, illumination conditions, and stereo calibration procedures were defined according to state-of-the-art best practices for DIC.[70] The MatchID® software and toolbox were used for image post-processing and strain evaluation.

Thermal stability and solvent resistance: Thermal stability of 3D-printed cross-linked polystyrene constructs was determined via thermogravimetric measurements (TGA 8000, PerkinElmer) and compared to linear bulk polystyrene. The analysis was carried out under inert atmosphere (constant nitrogen flow, 30,0 mL/min). The heating ramp was set from 30 to 800 °C with a heating rate of 15 °C/min. The ramp started after 5 minutes thermal equilibration of the samples at 30 °C. Solvent resistance was evaluated against acetone for both printed samples and bulk linear PS. For printed samples, the resistance was determined as the weight loss after 24 hours soaking following 6 hours drying at 80 °C. Weight loss was not determined for linear polystyrene as the samples dissolved completely after 24 hours.

Open Access Article. Published on 12 May 2026. Downloaded on 5/15/2026 10:57:01 AM.
This article is licensed under a Creative Commons Attribution 3.0 Unported Licence.

Materials Horizons Accepted Manuscript

View Article Online
DOI: 10.1039/D6MH00331A

Results and discussion

Oil-in-water high internal phase emulsions (HIPEs) were prepared in four formulations, each with a constant oil volume fraction of 0.85 and varying methacrylated dextran (DexMA) content in the aqueous phase (0, 1, 3, and 5 wt/v%). The detailed composition is reported in the Experimental Section. HIPEs were obtained by the controlled, dropwise addition of the hydrophobic phase into the aqueous phase under continuous stirring. Methacrylated dextran was synthesized by functionalizing dextran according to a previously reported method,[21,22] yielding a degree of methacrylation of 25%.

Macroscopically, all HIPEs exhibited pronounced viscoelasticity and high yield stress, as evidenced by their resistance to flow when the formulation vial was tilted. Confocal microscopy confirmed the formation of the characteristic jammed structure associated with HIPEs (**Supporting Figure 1**), where the dispersed oil domains exceed the theoretical packing limit of 0.74.[23,24] For imaging, Dextran functionalized with fluorescein isothiocyanate (FITC-Dextran) was introduced in the aqueous phase while the oil phase was stained with Nile Red. Morphological analysis revealed that both the mean droplet radius and polydispersity index decreased with increasing DexMA content (Supporting Figure 1). This trend is consistent with the relationship:[25]

$$R \propto \frac{\gamma_i}{\eta_{\text{eff}}(\dot{\gamma})\,\dot{\gamma}} \text{ (for } Ca \geq Ca_{\text{crit}}\text{)}$$

where R is the droplet radius, γ_i the oil–water interfacial tension, and $\eta_{\text{eff}}(\dot{\gamma})$ the shear-dependent viscosity of the continuous phase that accounts for the non-Newtonian nature of the glycerol-, surfactant- and DexMA-containing water phase. When the critical capillary number (Ca_{crit}) is exceeded, the initially large oil drops elongate into cylinders and subsequently break into smaller droplets.[26] A higher DexMA content in water translates into an increase in the viscosity of the external phase,[27] which enhances droplet breakup, resulting in finer and more uniform HIPE microstructures.[28]

A preliminary rheological characterization using a cone-plate geometry revealed that all HIPE-based formulations exhibit pronounced elasticity and high viscosity, accompanied by a strong shear thinning behaviour. Amplitude sweep tests showed high storage modulus values (*G'*, around 400 Pa) in the linear viscoelastic region (**Supporting Figure 2**), indicating a highly structured network capable of resisting deformation under moderate strains. Rotational flow experiments confirmed that viscosity decreases markedly with increasing shear rate (**Supporting Figure 3**), a feature essential for extrusion-based 3D printing as it ensures smooth flow through the nozzle while maintaining structural integrity

Open Access Article. Published on 12 May 2026. Downloaded on 5/15/2026 10:57:01 AM.
This article is licensed under a Creative Commons Attribution 3.0 Unported Licence.

Materials Horizons Accepted Manuscript

View Article Online
DOI: 10.1039/D6MH00331A

at rest.[29] These properties (high elasticity at low strain and shear-thinning under flow) are fundamental prerequisites for printability.[30] However, conventional rheological metrics provide only a partial view of material behaviour and cannot fully capture the dynamic sequence of stresses and deformations that occur during printing.[31] Extrusion is not a single event but a continuum of processes that can be conceptually mapped onto four stages:[32,33] i) the ink rests in the syringe in its most structured state; ii) pressure initiates flow and triggers yielding; iii) the ink accelerates through a contraction and then a narrow nozzle, undergoing intense shear that fluidizes its microstructure; iv) finally, once deposited, the ink must rapidly recover elasticity to maintain shape fidelity. These transitions (*i.e.,* from solid-like to fluid-like and back) are central to printability yet are not described by steady-state or small-amplitude oscillatory tests.[31]

Large-amplitude oscillatory shear (LAOS) experiments replicate this sequence of deformation and relaxation,[34] subjecting the material to alternating phases of loading, yielding, viscous flow, and recovery, conditions that closely mirror those encountered during extrusion. Several approaches have been proposed to interpret non-linear viscoelastic responses under LAOS, the most widely used being Fourier transform (FT) rheology[35–37] and the Chebyshev polynomial decomposition of elastic and viscous stresses.[38,39] FT rheology decomposes the stress waveform into a series of harmonics in the frequency domain, providing a "fingerprint" of non-linearity,[40] while the Chebyshev approach expresses the stress response as an orthogonal polynomial series enabling the definition of intra-cycle measures such as strain stiffening or shear thinning.[39,41] Although mathematically rigorous, both methods rely on global averages or harmonic coefficients that mix elastic and viscous contributions, which makes their physical interpretation challenging, especially when transient processes such as yielding and recovery dominate the response.[42]

Firstly proposed by Rogers in 2012,[43] the sequence of physical processes (SPP) approach overcomes these limitations by treating the stress response as a trajectory in a three-dimensional deformation space defined by strain, strain rate, and stress. **Figure 2**, panel A.iii shows the deformation trajectory of a 3% DexMA HIPE at two different strain amplitudes as an example.[44] This trajectory is analysed via differential geometry within the Frenet-Serret framework.[45,46] At any point along the deformation trajectory, three orthonormal vectors are constructed: $\vec{T}$ (tangent), indicating the instantaneous direction of motion along the curve; $\vec{N}$ (normal), pointing toward the direction of curvature (how the trajectory bends);

Open Access Article. Published on 12 May 2026. Downloaded on 5/15/2026 10:57:01 AM.
This article is licensed under a Creative Commons Attribution 3.0 Unported Licence.

Materials Horizons Accepted Manuscript

View Article Online
DOI: 10.1039/D6MH00331A

$\vec{B}$ (binormal), orthogonal to both $\vec{T}$ and $\vec{N}$ and defining the orientation of the osculating plane (which is in turn defined by the first two vectors). From these vectors, the orientation of the trajectory can be used to compute the transient elastic and viscous moduli (G'_t and G''_t), which represent the instantaneous contribution of strain and strain rate to the stress response. The complete derivation of the instantaneous moduli is provided in the Experimental Section and referenced elsewhere.[43] Unlike global measures, these moduli evolve continuously throughout the oscillation, capturing the material's transitions between solid-like and fluid-like states. When plotted as Cole-Cole curves (G'_t vs. G''_t), the trajectory typically forms a deltoid shape (Figure 2, panel A.iii) whose vertices correspond to critical stages of the printing process:[47] maximum elasticity at rest, yielding onset, full fluidization under high strain rate, and finally recovery (this correspondence is schematically illustrated in Figure 2, panels A and B). This approach provides a physically meaningful, time-resolved description of non-linear viscoelasticity, making it particularly suited for predicting printability.[34]

Open Access Article. Published on 12 May 2026. Downloaded on 5/15/2026 10:57:01 AM.
This article is licensed under a Creative Commons Attribution 3.0 Unported Licence.

Materials Horizons Accepted Manuscript

View Article Online
DOI: 10.1039/D6MH00331A

Open Access Article. Published on 12 May 2026. Downloaded on 5/15/2026 10:57:01 AM.
This article is licensed under a Creative Commons Attribution 3.0 Unported Licence.

Materials Horizons Accepted Manuscript

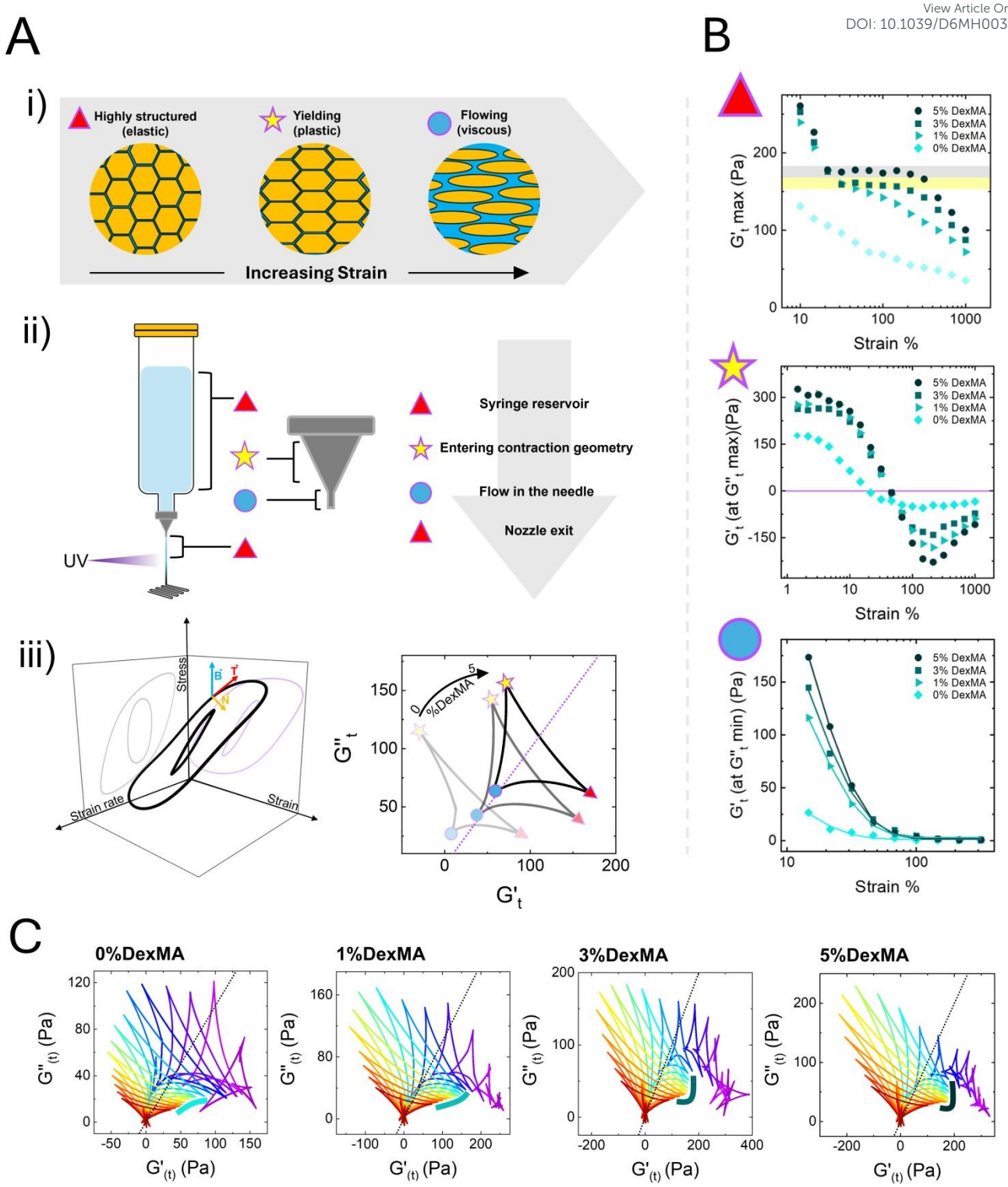

Figure2. Nonlinear rheological analysis. **A(i)** Structural transitions of HIPE-based inks under increasing strain, from highly structured (elastic) to yielding and fully fluidized (viscous). Symbols indicate each state and are used throughout the figure to link rheological data to printing stages. At rest, oil domains are tightly packed, and elasticity is at its maximum. As strain increases, domains elongate in the direction of deformation (yielding), and at sufficiently high strain, reciprocal sliding occurs, enabling viscous flow. **A(ii)** Schematic of the extrusion process, mapping structural states to syringe reservoir, contraction zone, nozzle passage, and exit. Each stage corresponds to a specific rheological regime and structural arrangement of the HIPE. **A(iii)** Left: Example of 3D deformation trajectories for 3% wt/v DexMa HIPE at 6.81% and 21.5% strain (5 rad/s), shown as projections

View Article Online
DOI: 10.1039/D6MH00331A

in strain–strain rate–stress space. These trajectories are constructed from strain/stress and strain rate/stress Lissajous plots and can be described by three orthonormal vectors (T, N, B), enabling calculation of instantaneous moduli (*G'ₜ, G''ₜ*) at any point in the cycle. Right: Cole–Cole plots (*G'ₜ* vs. *G''ₜ*) for representative samples (0%, 1%, 3% and 5% DexMa, strain 31.6%, 5 rad/s). Each deltoid vertex corresponds to a different printing stage and structural state of the HIPE-based ink. **B:** Summary of SPP analysis for samples with 0%, 1%, 3%, and 5% wt/v DexMa at 5 rad/s. From top to bottom: (i) $G'_{t\,\max}$ vs. strain (indicator of elastic recovery after extrusion), (ii) G'_tat $G''_{t\,\max}$ vs. strain (sharpness of the transition during flow initiation in the contraction zone), and (iii) G'_tat G''_tmin vs. strain (residual elasticity at maximum strain, reflecting structural integrity under high deformation). **C** Cole–Cole plots (*G'⍁ vs. G"⍁*) for HIPE-based inks containing 0%, 1%, 3%, and 5% wt/v DexMA in the aqueous phase, plotted counterclockwise with increasing strain amplitude (6.81–1000%). Each deltoid represents the intra-cycle evolution of viscoelastic response under LAOS. Highlighted regions on the lower part of the trajectories indicate a "vertical plateau" in $G'⍁_{\max}$ for formulations with DexMA ≥1%, where elasticity remains nearly constant despite progressively increasing strain, suggesting enhanced structural stabilization under large deformations.

Indeed, Jeong et al.[47] recently suggested that the values of *G'ₜ* at the vertex of the *G'ₜ* vs. *G''ₜ* Cole-Cole deltoids can be associated with the behaviour of a structured viscoelastic fluid during the printing process. Specifically, $G'_{t\,max}$ (*i.e.,* the maximum value of *G'ₜ*, indicated with a red triangle in Figure 2) is relative to the maximum elasticity of the sample at lower strains (representative of the material state in the syringe reservoir and immediately after exiting the extrusion nozzle). Higher values of $G'_{t\,max}$, can be related to an improved elastic response of the extruding fluid, implying that the ink retains a robust structure under repeated flow-rest cycles, contributing to both storage stability and rapid post-extrusion recovery. *G'ₜ* at $G''_{t\,max}$ (indicated as a yellow star in Figure 2) describes the sharpness of elastic yielding. More negative values indicate a stronger elastic inversion, reflecting a faster and more abrupt transition from a solid-like to a fluid-like state, thereby pointing towards a more rapid flow initiation upon entering the contraction channel. Finally, *G'ₜ* at $G''_{t\,min}$ (indicated as a light-blue circle in Figure 2) is relative to the residual elasticity of the ink at maximum strain, *i.e.,* when it's completely fluidized. Higher values of *G'ₜ* at $G''_{t\,\max}$ may indicate an excess in elasticity which can cause inward tension of the filament (a recoil-like behaviour). This residual tension can induce flow retraction of the filament thereby affecting the resolution of the printed object.

The contribution of DexMA to said rheological parameters is summarized in Figure 2, panel B. From top to bottom, $G'_{t\,max}$, *G'ₜ* at $G''_{t\,max}$, and *G'ₜ* at $G''_{t\,min}$ are reported as a function of strain % and for DexMA content varying from 0% to 5%. All the plots are relative to a fixed frequency of 5 rad/s. As shown in Figure 2.B, top panel, $G'⍁_{max}$ increases significantly in the presence of DexMA. At 100% strain, values rise from ~70 Pa for 0% DexMA to over 150 Pa for 1% DexMA. Further increases in DexMA content continue to elevate $G'⍁_{max}$ at

Open Access Article. Published on 12 May 2026. Downloaded on 5/15/2026 10:57:01 AM.
This article is licensed under a Creative Commons Attribution 3.0 Unported Licence.

Materials Horizons Accepted Manuscript

View Article Online
DOI: 10.1039/D6MH00331A

comparable strain levels, albeit with a less pronounced slope. An intriguing feature is the emergence of a plateau in the G'_{max} vs. strain curve for samples containing 3% and 5% DexMA. This plateau becomes more extended as DexMA concentration increases, suggesting a polymer-induced stabilization effect in the continuous phase. Similar phenomena have been reported for polymer-thickened systems, where macromolecular entanglements enhance elastic recovery under deformation.[48,49] From a practical standpoint, this behaviour indicates that DexMA contributes positively to storage stability and post-extrusion shape retention. As reported in Figure 2.B, middle panel, G' at G''_{max} exhibits an initial plateau at low strain, followed by an exponential decrease. For the DexMA-free sample, this decline begins around 5% strain, whereas for DexMA-containing formulations (1-5% wt/v), the onset occurs later and follows a similar trend across compositions. Notably, the DexMA-free sample reaches negative G' values at lower strain, implying easier flow initiation under moderate shear rates during nozzle contraction. In contrast, DexMA-containing samples display increasingly negative values at high strain, indicating that after an initial resistance, polymer chain alignment facilitates flow—a phenomenon analogous to shear thinning. This suggests that DexMA enhances the formulation's adaptability to extrusion while maintaining structural integrity. The bottom panel shows that G' at G''_{min} decreases for all samples as strain increases from intermediate (~12%) to 100%, eventually converging to small positive values. This indicates that none of the formulations exhibit significant recoil tendencies. However, residual elasticity, though minimal, still scales with DexMA content (close-up of the graph in **Supporting Figure 4**), likely due to viscosity enhancement in the continuous phase. Such viscosity-driven stabilization under stress has been previously observed in HIPE systems.[17] Residual elasticity may thus serve as an indicator of structural integrity preservation, particularly the tight packing of oil domains, which underpins the pronounced elasticity of HIPEs both at rest and under load.

Nonlinear rheological analysis, interpreted through the lens of printability for DexMA-containing formulations, indicates that the most promising system is the one incorporating 5% wt/v DexMA. To validate this prediction, following standard literature protocols, we first performed 2D printability tests to assess the dependence of printing resolution on ink composition, and then conducted qualitative 3D experiments aimed at evaluating overall shape fidelity prior to UV-induced crosslinking of DexMA. An in-house 3D printer was employed for the fabrication process. The printer is equipped with four optical waveguides

Open Access Article. Published on 12 May 2026. Downloaded on 5/15/2026 10:57:01 AM.
This article is licensed under a Creative Commons Attribution 3.0 Unported Licence.

Materials Horizons Accepted Manuscript

View Article Online
DOI: 10.1039/D6MH00331A

connected to a UV light source, arranged symmetrically around the nozzle tip to ensure homogeneous UV illumination (**Figure 3**, panel A). The ink is loaded into a metallic syringe, and its flow is pneumatically regulated via a microfluidic controller connected to a nitrogen source. Technical details of the printing system components are described in the Experimental Section.

In the 2D tests (filament fusion test,[50] see Experimental Section and Supporting Information), image analysis of serpentine filaments deposited at progressively increasing spacing revealed no significant difference in resolution among the inks, suggesting that the addition of DexMA does not measurably affect two-dimensional printing accuracy (**Supporting Figure 5**). However, the behaviour of inks with varying DexMA content diverged markedly in 3D layer-by-layer deposition trials. Here, the differences in elasticity of DexMA (both at rest and under stress, as previously highlighted by rheology and proportional to DexMA concentration) translated into visibly superior shape retention for the formulation with the highest DexMA content (Figure 3C, left). This macroscopic observation corroborates rheological predictions, which anticipated enhanced structural integrity of the high internal phase emulsion at elevated DexMA concentrations, particularly in the 5% wt/v DexMA formulation. Maintaining the internal architecture of the concentrated emulsion during printing is crucial for preserving full homogeneity in the final material, thereby preventing phase separation and the uncontrolled formation of segregated polymeric domains that would compromise the mechanical properties of the polymerized construct. Nevertheless, even at 5%DexMA, shape fidelity is not absolute, but this limitation is effectively mitigated by our printing strategy. During extrusion, the thin layer of continuous phase undergoes rapid UV crosslinking, forming a supporting hydrogel scaffold that fully stabilizes the structure. As shown in Figure 3 (panel C, middle) UV exposure during extrusion/deposition dramatically enhances printing fidelity across all formulations, with improvements scaling with DexMA content. This trend reflects the role of DexMA in forming the external crosslinked network that confers immediate structural reinforcement. Despite the clear positive contribution of DexMA, it is important to note that in this study only its concentration in the continuous phase varied, while the degree of methacrylation remained constant at approximately 25%. Consequently, aqueous solutions containing different amounts of fully cross-linked DexMA would form hydrogel networks of different densities, resulting in different extents of shrinkage upon curing. Excessive crosslinking could induce significant contraction of the external phase, potentially causing syneresis (expulsion of

Open Access Article. Published on 12 May 2026. Downloaded on 5/15/2026 10:57:01 AM.
This article is licensed under a Creative Commons Attribution 3.0 Unported Licence.

Materials Horizons Accepted Manuscript

View Article Online
DOI: 10.1039/D6MH00331A

water)[51,52] or, in extreme cases, acting like an over-compressed sponge that forces the oil phase (styrene and divinylbenzene) out of its compartments and toward the surface of the printed filament.

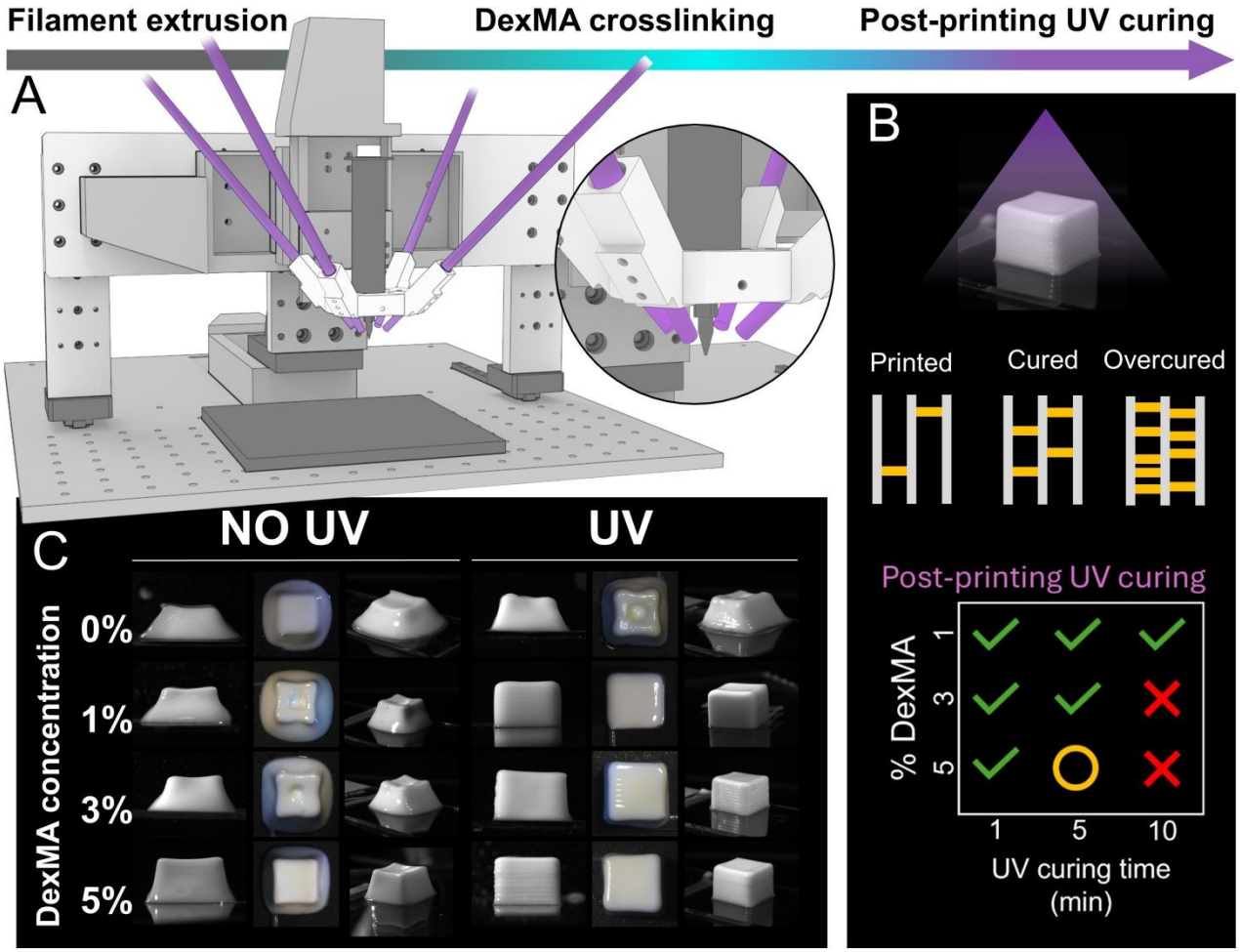

Figure 3. UV-assisted stabilization of HIPE-based inks during and after extrusion. **A**: custom-built extrusion platform equipped with four UV optical fibres positioned around the nozzle to enable in-situ crosslinking of the DexMA continuous phase during deposition. The inset highlights the nozzle region and UV irradiation geometry. **B**: post-printing UV curing: following the printing stage, during which constructs are exposed to continuous low-intensity UV, they are subjected to additional curing in a UV chamber for 1-10 min. Excessive curing leads to over-crosslinking and oil-phase leakage. The summary chart (bottom) summarizes optimal post-printing UV curing times for each formulation (*green thick*: no oil leakage; *yellow circle*: minimal oil leakage; *red cross*: extended oil leakage). As expected, lower DexMA concentrations tolerate extended curing, while the 5% wt/v DexMA sample requires minimal exposure (1 min) to avoid over-crosslinking and internal phase expulsion. **C**: Influence of DexMA concentration and UV exposure on 3D shape fidelity. Constructs printed without UV exhibit a progressive improvement in dimensional stability with increasing DexMA content, consistent with rheological predictions that higher polymer concentration enhances elasticity and recovery. Under UV exposure, all formulations show markedly improved fidelity, with the 5% DexMA ink producing near-perfect cubic geometries.

Open Access Article. Published on 12 May 2026. Downloaded on 5/15/2026 10:57:01 AM.
This article is licensed under a Creative Commons Attribution 3.0 Unported Licence.

Materials Horizons Accepted Manuscript

View Article Online
DOI: 10.1039/D6MH00331A

To prevent such undesired effects, precise control of UV exposure during printing is essential.[53] For all formulations, we standardized the process by employing four UV optical fibres operating at the minimum power allowed by the system (5% of the available intensity, see Experimental Section). This level of irradiation proved sufficient to maintain the structural fidelity of simple cubic constructs. To further enhance stabilization before thermal polymerization of the internal phase, printed samples were subjected to additional UV exposure in a curing chamber for progressively increasing intervals of 1, 5, and 10 minutes. As shown in **Supporting Figure 6** and schematically summarized in Figure 3, the 5% wt/v DexMA sample exhibited visible oil leakage after more than one minute of post-print curing, likely due to excessive crosslinking of the external DexMA network. Consistently, the 3% wt/v DexMA formulation showed leakage only after 5 minutes, whereas the 1% wt/v DexMA sample remained stable across all tested intervals. Considering the trade-off between rheological performance, layer-by-layer fidelity, and UV reactivity, we selected the 5% wt/v DexMA formulation for printing complex constructs under a standardized protocol: UV exposure at 5% power during extrusion, followed by a 1-minute curing step in the curing chamber. The constructs were then ready to be polymerized in an oven at 60°C for 6 hours to fully convert the oil phase into dense, cross-linked polystyrene.

The 5% wt/v DexMA formulation was initially employed to fabricate simple constructs, *i.e.,* cubic specimens with 1 cm edge length. Printing was performed following the UV-exposure protocol described above, using a pneumatic pressure of 40 mbar, which was empirically determined as the minimum required to deposit a continuous filament during preliminary 2D printability tests. After the complete process, including thermal curing at 60°C to polymerize styrene-divinylbenzene, the cubic constructs exhibited excellent shape fidelity compared to their counterparts exposed only to UV irradiation, negligible shrinkage (**Supporting Figure 7**) and demonstrated remarkable reproducibility (see **Figure 4**, panel A, for the uniformity of the replicated constructs). Quasi-static compression tests on parallelepiped specimens exhibited a smooth and continuous transition from the elastic regime to strain hardening, without the occurrence of a distinct yield plateau. A representative engineering stress-strain response is reported in **Supporting Figure 8**. From the initial linear region, the elastic modulus (E) was estimated to be approximately 850 MPa. Upon further deformation, the material sustained compressive stresses exceeding 100 MPa at strains of about 40% (0.4 mm/mm). The absence of brittle failure and the gradual increase in stress with strain suggest efficient stress redistribution across the sample, pointing towards the existence of a

Open Access Article. Published on 12 May 2026. Downloaded on 5/15/2026 10:57:01 AM.
This article is licensed under a Creative Commons Attribution 3.0 Unported Licence.

Materials Horizons Accepted Manuscript

View Article Online
DOI: 10.1039/D6MH00331A

multiscale organization in the tested material.[54] Scanning electron microscopy (SEM) analysis conducted on metallized samples (Figure 4, panel B) revealed a hierarchical architecture. At the macro/mesoscale the structure consists of distorted spherical poly(styrene-co-divinylbenzene) domains embedded within a thin dextran-based matrix. The size of these polymerized domains closely matches that of their liquid precursors in the original HIPE (diameters ranging from 4 to 8 μm, as determined by CLSM, Supporting Figure 1). This correspondence arises because the droplet size remains locked within the rapidly gelled aqueous phase during UV exposure upon extrusion, preserving the morphology of the HIPE template. Higher magnification revealed a second level of organization: each micrometric domain is composed of densely packed, highly monodisperse nanospheres (~200 nm in diameter). The packing density is so high that, at extreme magnification, the nanospheres appear deformed into hexagonal shapes, forming nearly perfect hexagonal close-packed (HCP) arrangements. This configuration, together with face-centred cubic (FCC), represents the most efficient packing mode for monodispersed spheres at the theoretical maximum volume fraction of 0.74.[55] The presence of these nanodomains is attributable to an emulsion polymerization mechanism of styrene, consistent with the well-known Harkins pathway[56,57] and previously observed in styrene-based oil-in-water HIPEs in our earlier work.[17]

A comparative analysis of the compressive properties of our printed samples against benchmark FDM polymers (ABS - Acrylonitrile Butadiene Styrene, and PETG – Polyethylene Terephthalate Glycol) was performed using values reported in the literature for specimens printed with the same infill density (100%) and identical layer deposition pattern,[58–60] ensuring meaningful comparison. As reported in Figure 4, panel C, our constructs exhibited yield stress values comparable to those of ABS and PETG, confirming the structural potential of the proposed dual-curing approach. More strikingly, the maximum compressive stress, defined as the peak stress on the stress-strain curve, was consistently more than twice that of the reference materials. This enhancement likely stems from superior interlayer cohesion achieved through *in situ* crosslinking of the HIPE ink's continuous phase during deposition. Unlike conventional FDM, where rapid cooling of extruded filaments limits thermal bonding and weakens interlayer adhesion, our strategy promotes robust fusion between adjacent layers. This effectively mitigates a critical failure mode in FDM-printed components *(i.e.*, interlayer delamination) enabling the fabrication of mechanically resilient structures. Moreover, being cross-linked, our constructs are inherently resistant to solvents

Open Access Article. Published on 12 May 2026. Downloaded on 5/15/2026 10:57:01 AM.
This article is licensed under a Creative Commons Attribution 3.0 Unported Licence.

Materials Horizons Accepted Manuscript

View Article Online
DOI: 10.1039/D5MH00331A

and exhibit increased thermal stability compared to linear polystyrene (**Supporting Figure 9**).

After confirming the fidelity of the ink and the reproducibility of the overall process through simple constructs, we proceeded to print four complex geometries, representing well-documented challenges in additive manufacturing:[61–63] (i) a twisted shape with rippled walls (Figure 4, panel D, left), (ii) an outward free-standing overhang at 45°, (iii) an inward free-standing overhang at 45°, and (iv) a fully closed spherical structure (Figure 4, panel D, right, from top to bottom). These complex constructs were printed with high fidelity to their CAD models, highlighting the ink's ability to withstand gravitational stresses during the fabrication of objects featuring steep overhangs or fully enclosed cavities. Notably, all shapes were produced via straightforward extrusion printing (**Supporting Video 1**) without the use of any supporting bath or sacrificial structures, a requirement for most techniques involving polymer printing.[64–67]

It is also important to emphasize that all complex constructs shown in Figure 4 consist of walls formed by a single filament of ink, making their resistance to vertical loads even more remarkable. This extraordinary performance likely stems from the interplay between the composition of the ink's external phase and its overall viscoelasticity. Upon extrusion, the ink is in its most fluid state, and deposition onto the underlying layer can induce slight filament spreading before the elastic recovery predicted by rheological data occurs. This spreading and recovery mechanism coincides temporally with the onset of crosslinking in the external phase, which remains partially uncrosslinked in the underlying filament or, in the case of free-standing overhangs, in adjacent filaments. Given the ink's ability to print suspended in air and nearly horizontally, it is highly plausible that adjacent filaments form interlayer crosslinked junctions, conferring exceptional structural stability and enabling the fabrication of geometries with challenging angles without the need for sacrificial supporting material (**Supporting Video 2**-**4**).

Open Access Article. Published on 12 May 2026. Downloaded on 5/15/2026 10:57:01 AM.
This article is licensed under a Creative Commons Attribution 3.0 Unported Licence.

Materials Horizons Accepted Manuscript

View Article Online
DOI: 10.1039/D6MH00331A

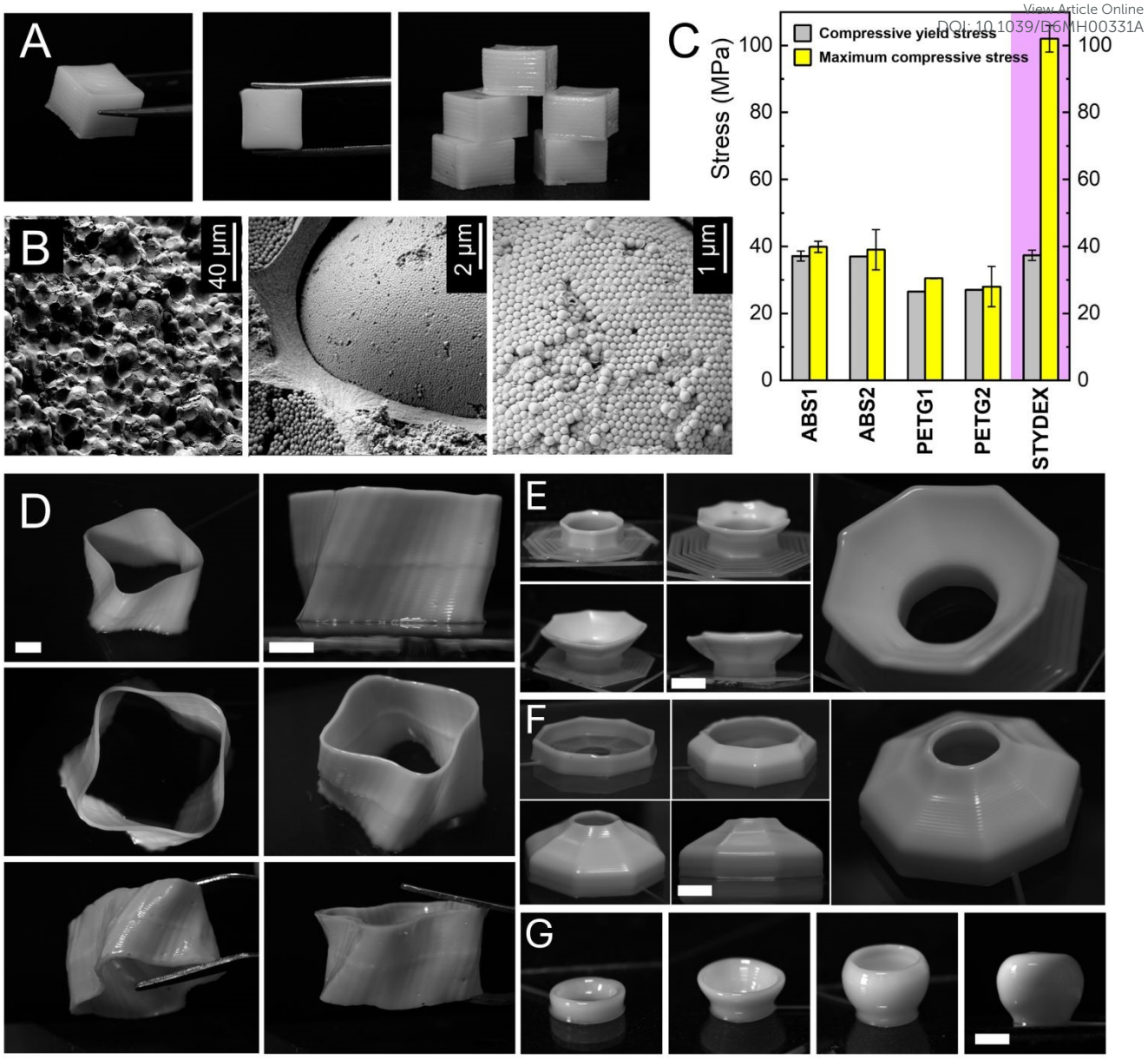

Figure 4. Printed constructs, hierarchical structure, and mechanical behaviour. **A**: polymerized cubic specimens highlighting the fidelity and reproducibility of the printing, curing, and polymerization process. **B**: SEM micrographs of the printed, fully polymerized material at different magnifications, revealing its hierarchical structure: from left to right, macro/mesoscale arrangement of poly(styrene-co-divinylbenzene) domains embedded in a thin DexMA, and detail of a single domain composed of densely packed nanospheres (~20 nm), forming highly ordered arrangements approaching hexagonal close packing. **C**: Comparison between yield stresses and maximum stresses of FDM printed constructs made of benchmark materials (ABS - Acrylonitrile Butadiene Styrene, and PETG – Polyethylene Terephthalate Glycol) and the same values calculated from the compressive mechanical tests conducted on our polymerized cubic specimens (STYDEX – highlighted in purple in the graph). Values for ABS and PETG are reproduced from recent literature: ABS1 (Kholil et al, 2022),[58] ABS2 (Mishra et al, 2024),[60] PETG1 (Zisopol, 2024),[59] PETG2 (Mishra et al, 2024).[60] In all the cited works, the specimens were produced with the same infill density (100%) and printing layer orientation used for the preparation for our tested samples. **D–E–F–G**: examples of challenging free-standing geometries fabricated using the 5% wt/v DexMA formulation, including twisted shapes with rippled walls (**D**), overhanging structures (outward overhang **E**, inward overhang **F**), and a hollow sphere (**G**). The multiple pictures of **E–F–G** refer to the same construct, captured at different printing stages or from different observation perspectives, to appreciate the inner and outer details and better visualize the objects' dimensions. All the

Open Access Article. Published on 12 May 2026. Downloaded on 5/15/2026 10:57:01 AM.
This article is licensed under a Creative Commons Attribution 3.0 Unported Licence.

Materials Horizons Accepted Manuscript

View Article Online
DOI: 10.1039/D6MH00331A

reported scale bars correspond to 1 cm. These constructs demonstrate the ink's ability to maintain dimensional fidelity under gravitational stress without the need for supporting baths; closed cavities, steep overhangs and multi-angles geometries underscore the synergy between ink viscoelasticity and interlayer crosslinking, enabling unprecedented design freedom for ambient-temperature printing of polystyrene.

Conclusions

We have demonstrated a strategy for ambient-temperature printing of polystyrene by decoupling the shape retention of the printed constructs from their polymerization kinetics. Incorporating methacrylated dextran (DexMA) into styrene/divinylbenzene HIPE inks enables rapid UV-induced crosslinking of the continuous phase during deposition, forming a stabilizing thin hydrogel scaffold while the oil phase undergoes subsequent thermal polymerization. This approach enables the printing of complex constructs at room temperature with high shape fidelity, overcoming the limitations of conventional thermoplastic processing. Non-linear rheology, interpreted through the sequence of physical processes (SPP) framework, revealed that DexMA concentration governs intracycle elasticity and recovery, directly correlating with printing performances. The formulation containing 5% wt/v DexMA (with respect to the water phase) provided the best performance, enabling free-standing geometries with challenging overhangs without the need for support structures. Importantly, this method enables the extrusion-based fabrication of crosslinked polystyrene, which is currently inaccessible to other techniques. The resulting constructs are inherently resistant to solvents and heating, making them promising for applications requiring chemical and thermal stability, such as filtration membranes, catalyst supports, and components for electrochemical devices. Beyond polystyrene, the same principle can be extended to other monomer-crosslinker systems. Decoupling shape retention from polymerization kinetics makes it feasible to combine inks with different monomer compositions, even those with widely different curing rates, within a single printing protocol. This opens the door to multi-material constructs and graded architectures with the potential to integrate functionalities that confer additional chemical or mechanical responsiveness. By leveraging HIPE modularity and multi-injection printing systems, this approach enables spatial control of composition and functionality without resorting to energy-intensive processing, thereby expanding the design space for advanced polymer additive manufacturing.

Open Access Article. Published on 12 May 2026. Downloaded on 5/15/2026 10:57:01 AM.
This article is licensed under a Creative Commons Attribution 3.0 Unported Licence.

Materials Horizons Accepted Manuscript

View Article Online
DOI: 10.1039/D6MH00331A

Author contributions

Vanessa Rosciardi: Conceptualization, Methodology, Software, Data curation, Investigation, Formal analysis, Writing - original draft, Writing - review & editing. *Federico Serpe*: Investigation, Methodology, Data curation, Writing - original draft, Formal analysis, Visualization, Conceptualization, Writing - review & editing. *Luca Scozzafava*: Investigation, Methodology. *Yurii Promovych*: Methodology, Resources. *Marco Costantini*: Writing - review & editing, Validation, Resources. *Marco Sasso*: Investigation, Validation, Funding acquisition. *Carlo Sabbatini*: Investigation, Formal analysis. *Roberta Angelini*: Supervision, Funding acquisition, Writing - review & editing. *Andrea Barbetta*: Conceptualization, Funding acquisition, Supervision, Writing - review & editing, Methodology, Project administration.

Conflicts of interest

The authors declare no competing financial interests or personal relationships that could have appeared to influence the work reported in this paper.

Data Availability

Additional experimental data are provided in Supporting Information. The Python code used for the Sequence of Physical Processes (SPP) analysis is deposited on GitHub available at https://github.com/vanessarosciardi/LAOS_SPP. A Zenodo DOI has been assigned to this repository, and it is available at https://doi.org/10.5281/zenodo.18681438. Raw datasets are available from the authors upon reasonable request.

Acknowledgments

CNIS (Research Center for Nanotechnologies Applied to Engineering, Sapienza University of Rome) is gratefully acknowledged for providing access to scanning electron microscopy (SEM) facilities and technical support. Giancarlo Ruocco, Simone De Panfilis and the Center for Life Nano- & Neuro- Science – CLN2S, IIT (Italian Institute of Technology, Rome) are gratefully acknowledged for providing access to confocal laser scanning microscopy (CLSM) facilities and technical support. A.B., R.A., and M.S. acknowledge financial support under the National Recovery and Resilience Plan (PNRR), Mission 4, Component 2, Investment

Open Access Article. Published on 12 May 2026. Downloaded on 5/15/2026 10:57:01 AM.
This article is licensed under a Creative Commons Attribution 3.0 Unported Licence.

Materials Horizons Accepted Manuscript

View Article Online
DOI: 10.1039/D6MH00331A

1.1, Call for tender No. 104 published on February 2, 2022 by the Italian Ministry of University and Research (MUR), funded by the European Union − NextGenerationEU − Project PRIN 2022ZA77J2 ICARUS − CUP B53D23009010006. A.B acknowledges financial support from Sapienza University of Rome, Ateneo 2024 funds, N°RM12419112CDC234. F.S. acknowledges financial support from Sapienza University of Rome, *Avvio alla Ricerca*, grant n° AR22419078AC2B88. V.R. acknowledges financial support under the National Recovery and Resilience Plan (PNRR), Mission 4, Component 2, Investment 1.2, Young Researchers – project SOE2024_0000147, BiFuelleD, CUP B83C25001210005. This work was supported by the National Science Centre Poland (NCN) with OPUS 19, grant n° 2020/37/b/st8/02167 to M.C.

Open Access Article. Published on 12 May 2026. Downloaded on 5/15/2026 10:57:01 AM.
This article is licensed under a Creative Commons Attribution 3.0 Unported Licence.

Materials Horizons Accepted Manuscript

View Article Online
DOI: 10.1039/D6MH00331A

References

[1] S. S. Banerjee, S. Burbine, N. K. Shivaprakash, J. Mead, *Polymers* **2019**, *11*(2), 347; DOI 10.3390/polym11020347.

[2] S. Park, W. Shou, L. Makatura, W. Matusik, K. Fu, *Matter* **2022**, *5(1)*, 43-76; DOI 10.1016/j.matt.2021.10.018.

[3] R. Monzón Mario and Paz, in *Springer Handbook of Additive Manufacturing* (Ed.: A. and G. D. and K. C. and M. M. and P. M. and S. T. Pei Eujin and Bernard), Springer International Publishing, Cham, **2023**, pp. 571–584.

[4] P. Siemiński, in *Additive Manufacturing* (Eds.: J. Pou, A. Riveiro, J. P. Davim), Elsevier, **2021**, pp. 217–275.

[5] M. Al-Hussein, G. Strobl, *Macromolecules* **2002**, *35(5)*, 1672-1676; DOI 10.1021/ma011345k

[6] A. Sola, *Macromol Mater Eng* **2022**, *307*(10), 2200197; DOI 10.1002/mame.202200197

[7] Y. Li, Y. Fan, J. Ma, *Polym Degrad Stab* **2001**, *73(1)*, 163-167; DOI 10.1016/S0141-3910(01)00

[8] D. V. A. Ceretti, Y. W. Marien, M. Edeleva, A. La Gala, L. Cardon, D. R. D'hooge, *Sustainability (Switzerland)* **2022**, *14*(23), 15488; DOI 10.3390/su142315488.

[9] C. Li, C. Feng, L. Zhang, L. Zhang, L. Wang, *Polym Eng Sci* **2025**, *65*(2), 431-454; DOI 10.1002/pen.27038

[10] L. Li, Q. Lin, M. Tang, A. J. E. Duncan, C. Ke, *Chemistry – A European Journal* **2019**, *25*(46), 10768-10781; DOI 10.1002/chem.201900975

[11] C. W. Visser, D. N. Amato, J. Mueller, J. A. Lewis, *Advanced Materials* **2019**, *31*(46), 1904668; DOI 10.1002/adma.201904668

[12] X. Li, X. Xu, L. Song, A. Bi, C. Wu, Y. Ma, M. Du, B. Zhu, *ACS Appl Mater Interfaces* **2020**, *12*(40), 45493-45503; DOI 10.1021/acsami.0c11434

[13] G. Cidonio, M. Costantini, F. Pierini, C. Scognamiglio, T. Agarwal, A. Barbetta, *J Mater Chem C Mater* **2021**, *9*(37), 12489-12508; DOI 10.1039/D1TC02117F

Open Access Article. Published on 12 May 2026. Downloaded on 5/15/2026 10:57:01 AM.
This article is licensed under a Creative Commons Attribution 3.0 Unported Licence.

Materials Horizons Accepted Manuscript

[14] Y. Wang, F. Guo, H. Li, Z. Tang, Y. Cheng, W. Li, *Int J Biol Macromol* **2025**, *297*, 139975; DOI 10.1016/j.ijbiomac.2025.139975

[15] C. Duty, C. Ajinjeru, V. Kishore, B. Compton, N. Hmeidat, X. Chen, P. Liu, A. A. Hassen, J. Lindahl, V. Kunc, *J Manuf Process* **2018**, *35*, 526-537; DOI 10.1016/j.jmapro.2018.08.008

[16] H. Zhang, F. Ye, F. Chen, W. Yuan, W. Yan, *Addit Manuf* **2024**, *81*, 103992; DOI doi.org/10.1016/j.addma.2024.103992

[17] V. Rosciardi, F. Serpe, S. De Panfilis, A. Barbetta, R. Angelini, *J Colloid Interface Sci* **2026**, *706*, 139571; DOI 10.1016/j.jcis.2025.139571

[18] V. Charlot, A. Ibrahim, X. Allonas, C. Croutxé-Barghorn, C. Delaite, *Polym. Chem.* **2014**, *5*(21), 6236-6243; DOI 10.1039/C4PY00550C

[19] Y. Sun, L. Wang, Y. Ni, H. Zhang, X. Cui, J. Li, Y. Zhu, J. Liu, S. Zhang, Y. Chen, M. Li, *Nat Commun* **2023**, *14*(1), 245; DOI 10.1038/s41467-023-35929-y

[20] Z. Jiang, B. Diggle, M. L. Tan, J. Viktorova, C. W. Bennett, L. A. Connal, *Advanced Science* **2020**, *7*(17), 2001379; DOI 10.1002/advs.202001379

[21] C. Palocci, A. Barbetta, A. La Grotta, M. Dentini, *Langmuir* **2007**, *23*(15), 8243-8251. DOI 10.1021/la700947g

[22] W. N. E. van Dijk-Wolthuis, O. Franssen, H. Talsma, M. J. van Steenbergen, J. J. Kettenes-van den Bosch, W. E. Hennink, *Macromolecules* **1995**, *28*(18), 6317-6322; DOI 10.1021/ma00122a044

[23] N. R. Cameron, D. C. Sherrington, in *Biopolymers Liquid Crystalline Polymers Phase Emulsion*, Springer Berlin Heidelberg, Berlin, Heidelberg, **1996**, pp. 163–214.

[24] H. Gao, L. Ma, C. Cheng, J. Liu, R. Liang, L. Zou, W. Liu, D. J. McClements, *Trends Food Sci Technol* **2021**, *112*, 36-49; DOI 10.1016/j.tifs.2021.03.041

[25] C. F. Welch, G. D. Rose, D. Malotky, S. T. Eckersley, *Langmuir* **2006**, *22*(4), 1544-1550; DOI 10.1021/la052207h

[26] G. I. Taylor, *Proceedings of the Royal Society of London. Series A, Containing Papers of a Mathematical and Physical Character* **1934**, *146*(858), 501-523; DOI 10.1098/rspa.1934.0169

View Article Online
DOI: 10.1039/D6MH00331A

Open Access Article. Published on 12 May 2026. Downloaded on 5/15/2026 10:57:01 AM.
This article is licensed under a Creative Commons Attribution 3.0 Unported Licence.

Materials Horizons Accepted Manuscript

View Article Online
DOI: 10.1039/D6MH00331A

764 [27] V. Tirtaatmadja, D. Dustan, D. Boger, *J Non-Newton Fluid* **2001**, *97*(2), 295-301; DOI
765 10.1016/S0377-0257(00)00226-3

766 [28] S. Tripathi, A. Bhattacharya, R. Singh, R. F. Tabor, *Chem Eng Sci* **2017**, *174*, 290.

767 [29] P. A. Amorim, M. A. d'Ávila, R. Anand, P. Moldenaers, P. Van Puyvelde, V. Bloemen,
768 *Bioprinting* **2021**, *22*, e00129; DOI 10.1016/j.bprint.2021.e00129

769 [30] P. Wei, C. Cipriani, C.-M. Hsieh, K. Kamani, S. Rogers, E. Pentzer, *J Appl Phys* **2023**,
770 *134*(10), 100701; DOI 10.1063/5.0155896

771 [31] M. I. Calafel, M. Criado-Gonzalez, R. Aguirresarobe, M. Fernández, C. Mijangos,
772 *Mater. Adv.* **2025**, *6*(14), 4566-4597; DOI 10.1039/D5MA00019J

773 [32] A. Schwab, R. Levato, M. D'Este, S. Piluso, D. Eglin, J. Malda, *Chem Rev* **2020**,
774 *120*(19), 11028-11055; DOI 10.1021/acs.chemrev.0c00084

775 [33] M. E. Cooke, D. H. Rosenzweig, *APL Bioeng* **2021**, *5*(1), 011502; DOI
776 10.1063/5.0031475

777 [34] Y. Liu, M. Hildner, O. Roy, W. A. Van den Bogert, J. Lorenz, M. Desroches, K. Koppi,
778 A. Shih, R. G. Larson, *J Rheol (N Y N Y)* **2023**, *67*(4), 791; DOI 10.1122/8.0000612

779 [35] T. Liang, A. I. Isayev, J. Zhong, *Polymer (Guildf)* **2023**, *267*, 125670; DOI
780 10.1016/j.polymer.2022.125670

781 [36] E. García-Tuñón, R. Agrawal, B. Ling, D. J. C. Dennis, *Physics of Fluids* **2023**, *35*(1),
782 017113; DOI 10.1063/5.0128658

783 [37] D. M. Hoyle, D. Auhl, O. G. Harlen, V. C. Barroso, M. Wilhelm, T. C. B. McLeish, *J*
784 *Rheol (N Y N Y)* **2014**, *58*(4), 969-997; DOI 10.1122/1.4881467

785 [38] A. M. Le, M. Y. Erturk, J. Kokini, *J Food Eng* **2023**, *336*, 111193; DOI
786 10.1016/j.jfoodeng.2022.111193

787 [39] A. Eid, M. M. Khader, A. M. Megahed, *Open Physics* **2024**, *22*(1), 20240001; DOI
788 doi:10.1515/phys-2024-0001.

789 [40] D. J. da Silva, G. S. Michelini, R. C. L. de Sá, A. H. Ferreira, *Carbohydr Polym* **2026**,
790 *373*, 124598; DOI 10.1016/j.carbpol.2025.124598

791 [41] S. O. Ilyin, *Polymer Science Series A* **2015**, *57*(6), 910-923.

Open Access Article. Published on 12 May 2026. Downloaded on 5/15/2026 10:57:01 AM.
This article is licensed under a Creative Commons Attribution 3.0 Unported Licence.

Materials Horizons Accepted Manuscript

View Article Online
DOI: 10.1039/D6MH00331A

792 [42] Q. Zhang, L. Jiang, X. Sui, *Food Hydrocoll* **2023**, *135*, 108177; DOI
793 10.1016/j.foodhyd.2022.108177

794 [43] S. A. Rogers, *J Rheol (N Y N Y)* **2012**, *56*(5), 1129-1151; DOI 10.1122/1.4726083

795 [44] J. Choi, F. Nettesheim, S. A. Rogers, *Physics of Fluids* **2019**, *31*(7), 073107; DOI
796 10.1063/1.5106378

797 [45] J. D. Park, S. A. Rogers, *Physics of Fluids* **2020**, *32*(6), 063102; DOI
798 10.1063/5.0006792

799 [46] G. Arreaga, R. Capovilla, J. Guven, *Class Quantum Gravity* **2001**, *18*(23), 5065; DOI
800 10.1088/0264-9381/18/23/304

801 [47] E. H. Jeong, J. Choi, H. B. Park, J. W. Lee, S. Y. Bae, B. S. Kim, C. Yoon, J. D. Park,
802 *Advanced Science* **2025**, e07639; DOI 10.1002/advs.202507639

803 [48] S. O. Ilyin, *Polymers (Basel)* **2024**, *16*(17), 2458; DOI 10.3390/polym16172458

804 [49] J. C.-W. Lee, L. Porcar, S. A. Rogers, *AIChE Journal* **2019**, *65*(12), e16797; DOI
805 10.1002/aic.16797

806 [50] A. Ribeiro, M. M. Blokzijl, R. Levato, C. W. Visser, M. Castilho, W. E. Hennink, T.
807 Vermonden, J. Malda, *Biofabrication* **2018**, *10*(1), 014102; DOI 10.1088/1758-5090/aa90e2

808 [51] K. Ako, S. Elmarhoum, C. D. Munialo, *Food Hydrocoll* **2022**, *124*, 107346; DOI
809 10.1016/j.foodhyd.2021.107346

810 [52] Z. Qin, Y. Yang, Z. Zhang, F. Li, Z. Hou, Z. Li, J. Shi, T. Shen, *Gels* **2025**, *11*(10),
811 DOI 10.3390/gels11100780

812 [53] A. Barkane, O. Platnieks, M. Jurinovs, S. Kasetaite, J. Ostrauskaite, S. Gaidukovs,
813 Y. Habibi, *Polymers (Basel)* **2021**, *13*(8), 1195; DOI 10.3390/polym13081195

814 [54] W. Lu, Q. Zhang, F. Qin, P. Xu, Q. Chen, H. Wang, F. Scarpa, H.-X. Peng, *Appl Mater*
815 *Today* **2021**, *25*, 101222; DOI 10.1016/j.apmt.2021.101222

816 [55] I. Sanchez-Burgos, E. Sanz, C. Vega, J. R. Espinosa, *Physical Chemistry Chemical*
817 *Physics* **2021**, *23*(35), 19611-19626; DOI 10.1039/D1CP01784E

818 [56] W. D. Harkins, *J Chem Phys* **1945**, *13*(9), 381-382; DOI 10.1063/1.1724054

Open Access Article. Published on 12 May 2026. Downloaded on 5/15/2026 10:57:01 AM.
This article is licensed under a Creative Commons Attribution 3.0 Unported Licence.

Materials Horizons Accepted Manuscript

819 [57] L. Peng, M. Wu, J. Lu, A. Zhang, K. Zhang, S. Ma, *Langmuir* **2025**, *41*(4), 2651-2660;
820 DOI 10.1021/acs.langmuir.4c04437

821 [58] A. Kholil, E. Asyaefudin, N. Pinto, S. Syaripuddin, in *J Phys Conf Ser*, Institute Of
822 Physics, **2022**.

823 [59] D. G. Zisopol, M. Minescu, D. V. Iacob, *Engineering, Technology and Applied Science*
824 *Research* **2024**, *14*(2), 13592-13597; DOI 10.48084/etasr.7063

825 [60] V. Mishra, N. Bharat, V. Kumar, D. Veeman, M. Vellaisamy, *Phys Scr* **2024**, *99*(12),
826 125033; DOI 10.1088/1402-4896/ad8fe0

827 [61] J. Jiang, J. Stringer, X. Xu, R. Y. Zhong, *Int J Comput Integr Manuf* **2018**, *31*(10),
828 961-969; DOI 10.1080/0951192X.2018.1466398

829 [62] J. Ye, X. Lin, H. Lu, H. Shen, Z. Wang, Y. Zhao, *Structures* **2024**, *59*, 105699; DOI
830 10.1016/j.istruc.2023.105699

831 [63] H. Quan, T. Zhang, H. Xu, S. Luo, J. Nie, X. Zhu, *Bioact Mater* **2020**, *5*(1), 110-115;
832 DOI 10.1016/j.bioactmat.2019.12.003

833 [64] W. Hua, K. Mitchell, L. Raymond, B. Godina, D. Zhao, W. Zhou, Y. Jin, *ACS Biomater*
834 *Sci Eng* **2021**, *7*(10), 4736-4756; DOI 10.1021/acsbiomaterials.1c00910

835 [65] J. Zhao, N. He, *J Mater Chem B* **2020**, *8*(46), 10474-10486.

836 [66] G. Nayyar, C. B. Williams, T. E. Long, *Polymer (Guildf)* **2025**, *326*, 128355; DOI
837 10.1016/j.polymer.2025.128355

838 [67] K. Fu, *Acc Mater Res* **2025**, *6*(8), 921-926; DOI 10.1021/accountsmr.5c00156

839 [68] S. Andrieux, W. Drenckhan, C. Stubenrauch, *Langmuir* **2018**, *34*(4), 1581-1590; DOI
840 10.1021/acs.langmuir.7b03602

841 [69] A. Gleadall, *Addit Manuf* **2021**, *46*, 102109; DOI 10.1016/j.addma.2021.102109

842 [70] M. Sutton, F. Hild, *Exp Mech* **2015**, *55*(1), 1-8; DOI 10.1007/s11340-015-9991-6

View Article Online
DOI: 10.1039/D6MH00331A

Open Access Article. Published on 12 May 2026. Downloaded on 5/15/2026 10:57:01 AM.
This article is licensed under a Creative Commons Attribution 3.0 Unported Licence.

Materials Horizons Accepted Manuscript

View Article Online
DOI: 10.1039/D6MH00331A

Open Access Article. Published on 12 May 2026. Downloaded on 5/15/2026 10:57:01 AM.
This article is licensed under a Creative Commons Attribution 3.0 Unported Licence.

Data availability statement

Additional experimental data are provided in Supporting Information. The Python code used for the Sequence of Physical Processes (SPP) analysis is deposited on GitHub is available at https://github.com/vanessarosciardi/LAOS_SPP. A Zenodo DOI has been assigned to this repository, and it is available at https://doi.org/10.5281/zenodo.18681438. Raw datasets are available from the authors upon reasonable request.

Materials Horizons Accepted Manuscript